The Electrochemical Society
Advancing solid state & electrochemical science & technology
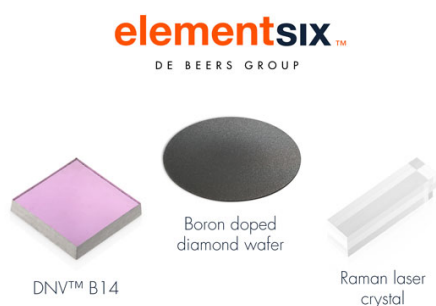
Developing Shunt-Current Minimized Soluble-Lead-Redox-Flow-Batteries

To cite this article: Rathod Suman *et al* 2021 *J. Electrochem. Soc.* **168** 120552

Developing Shunt-Current Minimized Soluble-Lead-Redox-Flow-Batteries

Rathod Suman, Satya Prakash Yadav, M. K. Ravikumar, [ID] Satish Patil, and A. K. Shukla[z] [ID]

Solid State and Structural Chemistry Unit, Indian Institute of Science, Bangalore—560012, India

Shunt currents in membrane-less soluble-lead-redox-flow-batteries (SLRFB) are observed in open-circuit condition and found to depend on size of the stack, manifolds, flow rates and charge/discharge parameters. Ramifications of shunt currents on the performance of membrane-less SLRFB stacks with internal and external manifolds are reported. In the case of stacks with 3, 5 and 7-cells and internal manifold design, the charge current for the middle cell decreases by 3.3%, 6%, and 8.5%, while the discharge current increases by 2.6%, 5.5%, and 6.6%, respectively, for 3 A charge/discharge current. By contrast, no such adverse effect is observed for external manifold design. The current—potential studies show that while the stacks comprising 3 and 5-cells deliver a maximum power density of 35 mW cm^{-2}, which declines to 15 mW cm^{-2} for the 7-cell stack with internal manifold design, while the power density remains invariant at 50 mW cm^{-2} for stacks with external manifold design. An 8-cell stack of 12 V, 50 mAh/cm^2 specific capacity and 273 Wh energy storage capacity with 64% energy efficiency is also reported which shows good cyclability over 100 cycles with 95% coulombic efficiency when cycled at 20 mA cm^{-2} current density for 1 h duration.
© 2021 The Electrochemical Society ("ECS"). Published on behalf of ECS by IOP Publishing Limited. [DOI: 10.1149/1945-7111/ac436c]

Large-scale energy storage systems have inevitable role to play in integrating renewable energy sources with main grid to achieve goals set by Paris Agreement on control of climate change.[1,2] The market forecast for such systems is estimated to be about US $ 10.51 billion US dollars by 2030.[3] Redox flow batteries systems have the flexibility in design to meet required power and energy characteristics making them attractive for such applications. They can also be deep discharged with high cycle life.[4–6] It is predicted that redox flow batteries will compete with Li-ion batteries for up to 69 GWh (46%) of the total 150 GWh of projected capacity in 2030.[7] Presently, Li-ion batteries and membrane divided redox flow battery systems are being installed in microgrids but have failed to penetrate on wider scale due to safety concerns, high cost and scarcity of raw materials. Soluble-lead-redox-flow-battery (SLRFB) is one of the low-cost emerging rechargeable flow battery technologies that can be used for large-scale energy storage applications in combining renewable energy sources with main grid.[8,9] Although the basic concept of SLRFB is known in the literature, there are no successful reports on performance characteristics of SLRFB stack with multiple cells.[10–19] By contrast, large stacks of allied redox flow battery (RFB) technologies, like all vanadium, Zn/Br$_2$, Fe/Cr, etc., have been designed, constructed, demonstrated, and even have reached the level of commercialization.[20,21] Even though these technologies have reached status of commercialization, the production, and maintenance costs remain high. It is noteworthy that SLRFB is based on abundant, low-cost materials and have option of developing it without the high-priced ion-exchange-membranes which make SLRFB more compelling among the redox flow battery systems for large scale energy storage applications.

Historically, Frits Beck first reported the development of soluble lead flow cells by depositing Pb and PbO$_2$ from lead perchlorate dissolved in perchloric acid electrolyte.[22] A more recent soluble lead flow cell is reported by Pletcher et. al based on lead methanesulfonate salts dissolved in methanesulfonic acid electrolyte.[10] Jie Cheng et al. have reported the performance characteristics of an all-lead redox flow battery in fluoroboric acid with Pb(BF$_4$)$_2$ and HBF$_4$ aqueous electrolyte.[23] Among these three systems, SLRFB described by Pletcher group is more suitable due to their chemical and electrochemical properties.[10–18,24,25] More recently, Pletcher et al. have reviewed the challenges faced with SLRFB technology.[26,27] It has been understood that the dendrites formed at anode and oxygen evolution from the cathode are the major problems in developing

soluble lead flow cells. These problems are associated with single electrodes and can be controlled by adding suitable additives.[28–31]

Research and development on stack of multiple-cell SLRFB is scanty in the literature. Wills et al, have reported a two-cell bipolar SLRFB with reticulated vitreous carbon (RVC) and Ni foam as electrode materials for cathode and anode, respectively; they have tested a two-cell stack only for 1 min charge and discharge schedules.[26,27] Oury et al. have reported a two cell SLRFB without using a bipolar plate and electrolyte was made to flow through one negative electrode into the graphite positive electrode having honeycomb shape.[19,27] Krishna et. al have reported that C—Tech Innovation Ltd. and University of Southampton had developed a 4-cell stack of SLRFB with about 1000 cm^2 active area but the shorting between the electrodes restricted its operation to 10 cycle; they have also reported that addition of sodium lignosulphonate together with hexadecyltrimethylammonium cation additive improves the performance of the stack to about 40 cycles. In addition to this, a 5-kWh pilot cell developed with Entegris carbon-polymer composite electrodes, Ni coated Pb anode and comprising 10 cells (frames) is also reported with active area of 400 × 250 mm.[27]

In the light of foregoing, it is surmised that development and performance testing of an undivided SLRFB stack remain a challenge. All the efforts made indicate that the development of a functional SLRFB stack hit a roadblock and the present study reflects that it could be due to negligence of shunt current and associated with manifold design and stack engineering requirements. Shunt current is ionic-leakage current observed in stacks of all electrochemical cells with common electrolyte manifolds, and it is an undesirable effect.[32] The effects of shunt current in redox-flow-batteries were first reported by NASA.[33] A direct ramification of the shunt current is the development of non-uniform voltage distribution across the stack. This leads to poor energy efficiency, decrease in cycle-life and failure of the stack.[34] Accordingly, understanding the origin of shunt current, its measurement and minimize it are mandatory for propelling the development of SLRFB.
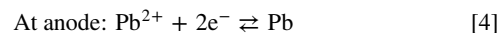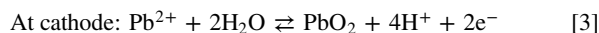
Shunt current is estimated either theoretically or experimentally. Theoretically, shunt current is estimated by modelling the stack as an analogous electrical network.[35–39] In this method, each cell of the stack is represented as series connected ideal voltage source. The electrolyte in channels and manifolds are considered as resistors in series/parallel combination. Subsequently, Kirchhoff's laws of electrical circuits are applied to derive linear equations involving unknown resistances for manifold and channel currents. The equations are then solved numerically to estimate the manifold and channel currents. There are three experimental techniques available

[z]E-mail: akshukla2006@gmail.com

to determine shunt currents. These are (a) measurement of shunt current using magnetic field detectors across the inlet/outlet of the electrolyte manifolds, (b) measurement of cell efficiency followed by calculating the shunt current, and (c) measurement of shunt current by placing inert electrode, like Pt electrode across the manifold and estimating the shunt current from the potential difference.[40] The magnetic field measurement method has limitation due to interference from magnetic field arising from dc current of the stack; the other two methods have limitations due to side reactions such as gas evolution and polarization effects due to activation, ohmic and concentration over-potentials. Since these methods are found to be prone to error, method described by Seiger is used in the present study to measure the internal electrical current distribution in SLRFB stack.[40] In this method, high precision *dc shunts* are inserted between electrode interconnects of each cell as well as at the terminal ends of the SLRFB stack to measure the internal electrical currents.

Origin of shunt current in membrane-less SLRFB and its measurement.—Figure 1 shows the schematic representation of (a) a membrane-less SLRFB single cell and (b) membrane-less SLRFB cells in series with channels and manifolds with *dc shunts* inserted between cells. Basically, a single cell of membrane-less SLRFB consists of three components namely—anode and cathode separated by an electrolyte flow frame having inlet and outlet for the electrolyte to get circulated. In the case of multiple cell stacks, cells are assembled using monopolar frames of anode, cathode and bipolar frames which can accommodate electrodes with independent current collectors. All the electrolyte flow frames are connected through common inlet and outlet manifolds. The electrical connection between anode and cathode of the bipolar frames are made only externally through high precision *dc shunts* and are labelled as S_1, S_2, S_3, etc.

In a membrane-less SLRFB single cell, during charging Pb^{2+}-ions are oxidized to Pb^{4+}-ions at the cathode and deposited as PbO_2 with the generation of electrons and protons. While electrons flow as electric current (I_e) to anode externally, H^+ flow across the electrolyte as ionic current (I_{ion}). The electrons and protons are utilized at the anode for the reduction of Pb^{2+}-ions to metallic lead. The corresponding electrode reactions are,

$$\text{At cathode: } Pb^{2+} + 2H_2O \rightleftarrows PbO_2 + 4H^+ + 2e^- \qquad [3]$$

$$\text{At anode: } Pb^{2+} + 2e^- \rightleftarrows Pb \qquad [4]$$

However, the flow cells do not have fixed volume of stationary electrolyte, but it is circulated through electrolyte flow frame, part of the ionic current (I_{ion}) escapes through the inlet and outlet of the electrolyte frames. This ionic current could reach adjacent cells through the flow-field channels and common manifolds causing them to exhibit mixed polarization effects. Since part of the ionic current is lost and only the remaining part is utilized at anode electrochemically lesser amounts of Pb and PbO_2 deposited during charge. During the discharge, this leaked ionic current adds up to the applied discharge current and increases dissolution rates of Pb and PbO_2. This leaking ionic current is generally termed as shunt current, parasitic current or bypass current.[35,36] It is noteworthy that even in open-circuit condition of a charged SLRFB, the ionic leakage current flows as long as the electrolyte is circulated through the stack.

When SLRFB cells are connected in series, the internal electric current that flows from cell to cell varies due to the leakage of ionic current through the channels and manifolds. The high precision dc shunts labelled as S_1, S_2, S_3, …S_n are inserted between the electrode interconnects of each cell as shown in Fig. 1b. These shunts are used to measure the internal electric current. It is a direct quantitative measurement of internal current flowing from cell-to-cell across the stack. The current flow through these shunts namely I_1, I_2, I_3 …, etc., are the internal currents flowing during charging/discharging of the SLRFB stack. The current I_1 flowing through S_1 represents the entry point for the flow of electrons into the stack while I_n flowing through the S_n is the point where electrons exit from the stack. The current I_2, I_3, I_4 …I_{n-1} flowing through the S_2, S_3, …S_{n-1} correspond to the internal currents across the stack. The difference between I_1 and I_2, I_3,….I_{n-1} is the magnitude of the current that leaks through the channels and manifolds. The sum of channel and manifold current is obtained by:

$$I_1 - I_2 = I_{1(ch+ma)} \qquad [5]$$

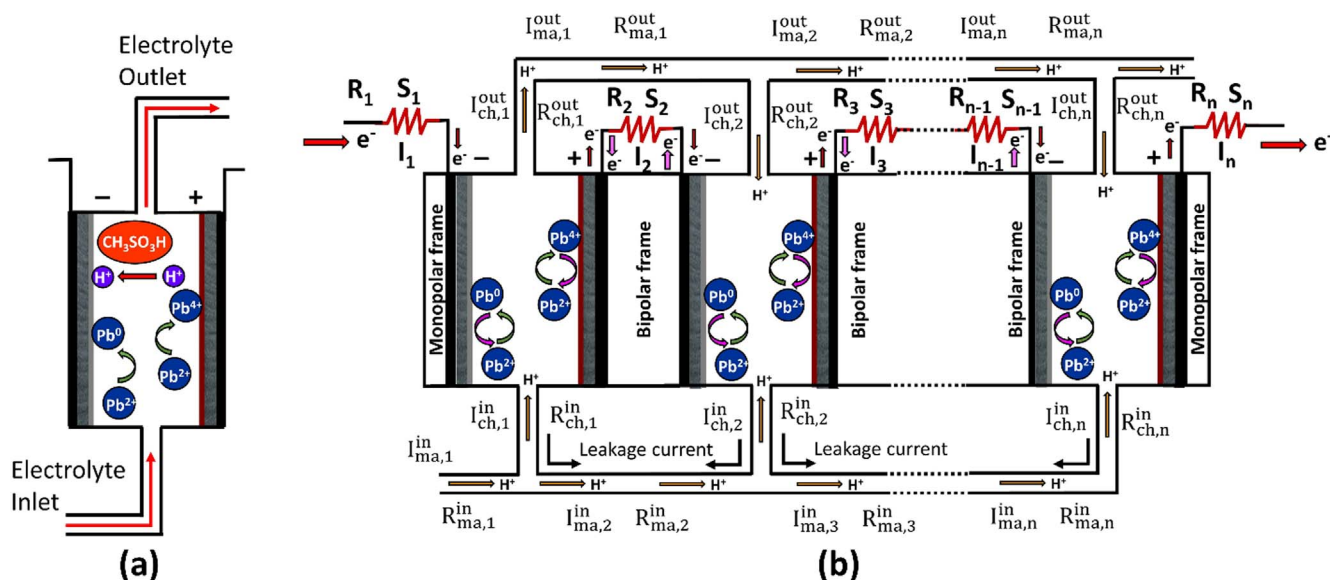$$I_1 - I_3 = I_{2(ch+ma)} \qquad [6]$$

and so on.

Figure 1. Schematics of (a) single SLRFB cell and (b) stack of SLRFB cells in series with dc shunts inserted between cell interconnects to measure internal current distribution.

where $I_{1(ch+ma)}$ is the sum of ionic currents leaking through the input and output of the channel and manifold of the electrolyte flow frame from cell 1 to cell 2. The leakage current is obtained from the difference between two adjacent shunts as follows:

$$I_1 - I_2 = I_{lc,1} \qquad [7]$$

$$I_2 - I_3 = I_{lc,2} \qquad [8]$$

and so on.

where $I_{lc,1}$, $I_{lc,2}$ and $I_{lc,3}$ are the ionic leakage currents from cell 1, cell 2 and cell 3, respectively.

The objectives of the present work are (a) to directly measure the internal current distribution and calculate the shunt current, (b) study the ramifications of shunt current in multicell stacks of SLRFB with internal and external manifold, (c) develop a functional membrane-less SLRFB stack of 12 V and study its performance characteristics. The present study is first of its kind in reporting the ramifications of shunt current in membrane-less SLRFB stacks and it reveals that the development of operational SLRFB stack relies on minimizing shunt current through proper stack design and engineering in addition to having additives to prevent Pb dendrites, PbO_2 sludge formation and reducing the rate of oxygen evolution reaction. Present study provides the guidelines on measuring and minimizing shunt current in SLRFB stacks and developing a fully functional stack of SLRFB which is presently lacking in the literature.

Experimental

Materials and components.—The materials and components, design details and electrolyte composition are described in detail elsewhere.[41,42] In brief, the electrolyte was prepared by dissolving 1 M of Lead (II) methane sulfonate in 0.5 M methane sulfonic acid. 100 mM of NaF and 5 mM of Hexadecyltrimethylammonium p-toluene sulphonate (HDTMA *p*-TS) were added as cathode and anode additives, respectively. NaF is added to reduce the oxygen evolution reaction and facilitate the strong adhesion of PbO_2 deposits at cathode, HDTMA *p*-TS is added to prevent Pb dendrite formation at anode. The effect of these additives and mechanism for the promotional effect are discussed elsewhere.[15,20,27,29,42,43] The combination of these two additives were chosen as they found to have good stability and long cycle of over 1300 cycles from the single cell studies.[42] 6 mm thick graphite felt (untreated) was used as electrode substrate. 3.8 mm thick impervious graphite plates attached with lead plated copper sheets of 0.2 mm thickness were used as current collectors. Polymethylmethacrylate (PMMA) sheets were used to make electrolyte and electrode frames. The active area of the electrode is 500 cm². The inter-electrode gap between the electrodes were 1.4 cm in internal manifold (IM) and 1.8 cm in the case of external manifold (EM) designs. The average internal resistance values of cells for internal and external manifold designs were found to be 0.015 Ω and 0.017 Ω respectively. The values were extracted using graphical method as described elsewhere.[44] The stack with internal manifold design was assembled with stainless steel end plates which were provided with inlet/outlet connectors for the electrolyte to be circulated. The stack inlet was linked to an electrolyte-tank through an electric-pump and the outlet was directly linked to the same electrolyte-tank. PVC tubing were used to circulate the electrolyte. In the case of external manifold stacks each electrolyte frame was provided with independent inlet and outlet. Silicone rubber tubes of ½ inch diameter and 1 m length were used as channels along with common electrolyte manifolds.

Figure 2 shows the schematic representation of the stacks with internal (Fig. 2a) and external (Fig. 2b) manifold designs. The major differences between the two designs are: (i) in external manifold design individual electrolyte flow frames have got independent electrolyte inlet and outlets (channels) whereas internal manifold design has a single inlet and single outlet ports through which electrolyte is distributed or collected through all cells and (ii) the

channel length in external manifold design is longer than in the case of internal manifold design. The shunt current depends on the resistance of the electrolyte (R) for the ions to flow from one cell to adjacent cell and it is defined by following equation, $R = \rho \frac{l}{A}$, where ρ is the resistivity, $l =$ length of the channel, $A =$ area of the cross section of the channel. In the external manifold design, we have the provision to increase the channel length or decrease the area of cross section of channel and there- by increase the resistance for the ions to flow across one channel to the other channel and hence to decrease in the shunt current. PVC flow control valves were used to regulate the flow rate and it was measured by collecting the electrolyte at outlet using the measuring cylinder over a particular time period. In case of internal manifold, the overall flow rate of the stack was controlled and in the case of external manifold flow rate was controlled in individual cells.

Electrochemical characterization.—3 and 5-cells SLRFB stacks were tested using a 20 V-100 A, BTS-2000 model battery testing system from Arbin Instruments, USA and 7-cell SLRFB stack was tested using a 100 V—300 A, FTV model battery cycler from Bitrode Corporation, USA. High precision *dc shunts* of 50 mV/150 A were procured from Murata Power Solutions Inc., USA. These shunts were made of manganin alloy element with a rated accuracy of 0.25% and have a resistance of 0.33 mΩ at 25 °C and their operating temperature range was—40 °C to + 60 °C. All the high precision *dc shunts* were connected to a Keithley switch system model 3706 having a high resolution of $7\frac{1}{2}$ digit accuracy to measure the voltage drop across the shunts and calculate the internal current distribution in the membrane-less SLRFB stack during their charge-discharge cycles. The data acquisition rate was 1 point per sec for all shunts. All equipment were connected through independent computers and operated through the software supplied by the OEM. The *dc shunts* were calibrated prior to their assembly into the stack.

The SLRFB stacks were activated galvanostatically by about 25 charge-discharge cycles at current density of 24 mA cm⁻² for 15 min charge durations and discharging to 0.8 V cut-off voltage per cell. Shunt current measurements were recorded for 5 min duration at varying charge-discharge current densities. The charge-discharge tests of SLRFB were carried out at varying current densities, varying time at different electrolyte flow rates. The current-potential polarization behavior of the single cell and stack were obtained by constant current polarization method. The charge-discharge data of all stacks were recorded with 1 h charge and discharging to 0.8 V cut-off voltage per cell. The coulombic, voltaic and energy efficiencies are calculated as described elsewhere.[21]

Results and Discussion

Internal current distribution in membrane-less SLRFB stacks.—The electric current that flows through *dc shunts* of 3, 5 and 7-cell SLRFB stacks with internal manifold and external manifold designs at open circuit condition after charging the stack for 5 min at 24 mA cm⁻² and at various flow rates are shown in Figs. 3a–3f. It is clearly observed from Fig. 3 that no current is flowing across at the terminal end shunts, namely S_1 and S_4 of the 3-cell stack, S_1 and S_6 of 5-cell stack, S_1 and S_8 in the case of 7-cell stack. Interestingly, a negative current is observed to be flowing across the interplaced *dc shunts* indicating that the intermediate cells could undergo self-discharge due to ionic-leakage current. The magnitude of this current is found to be higher in the middle cells. It is also noticed that the shunt current increases with the increase in the number-of-cells in the stack and flow rate of the electrolyte in the stacks of both internal and external manifold designs. However, the magnitude of the ionic leakage current is higher in the case of stacks with internal manifold than the stacks with external manifold. Typically, it can be noticed from Figs. 3a and 3d that the shunt current observed from the *dc* shunt S_2 in 3-cell internal manifold stack with 1.2 liters per minute (lpm) overall flow rate is found to be
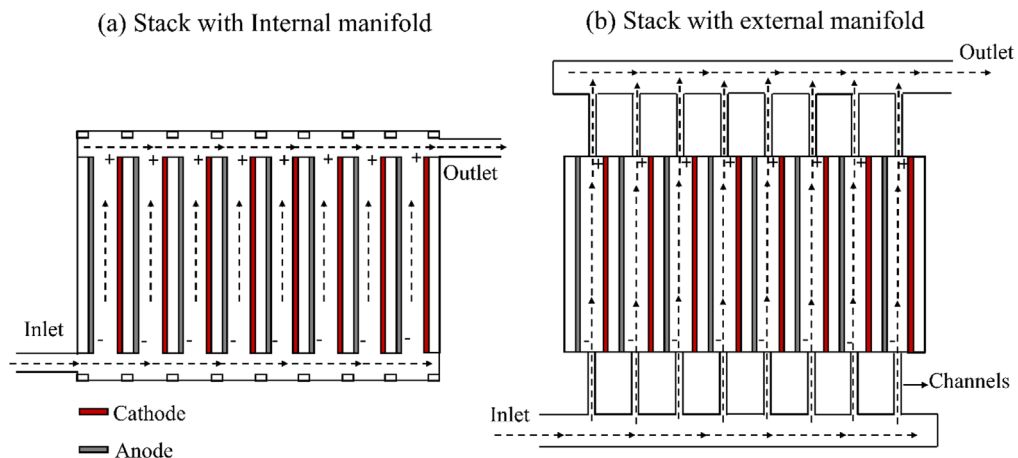
(a) Stack with Internal manifold (b) Stack with external manifold

Figure 2. Schematic representation of the SLRFB stacks with internal manifold design (a), and external manifold design (b).
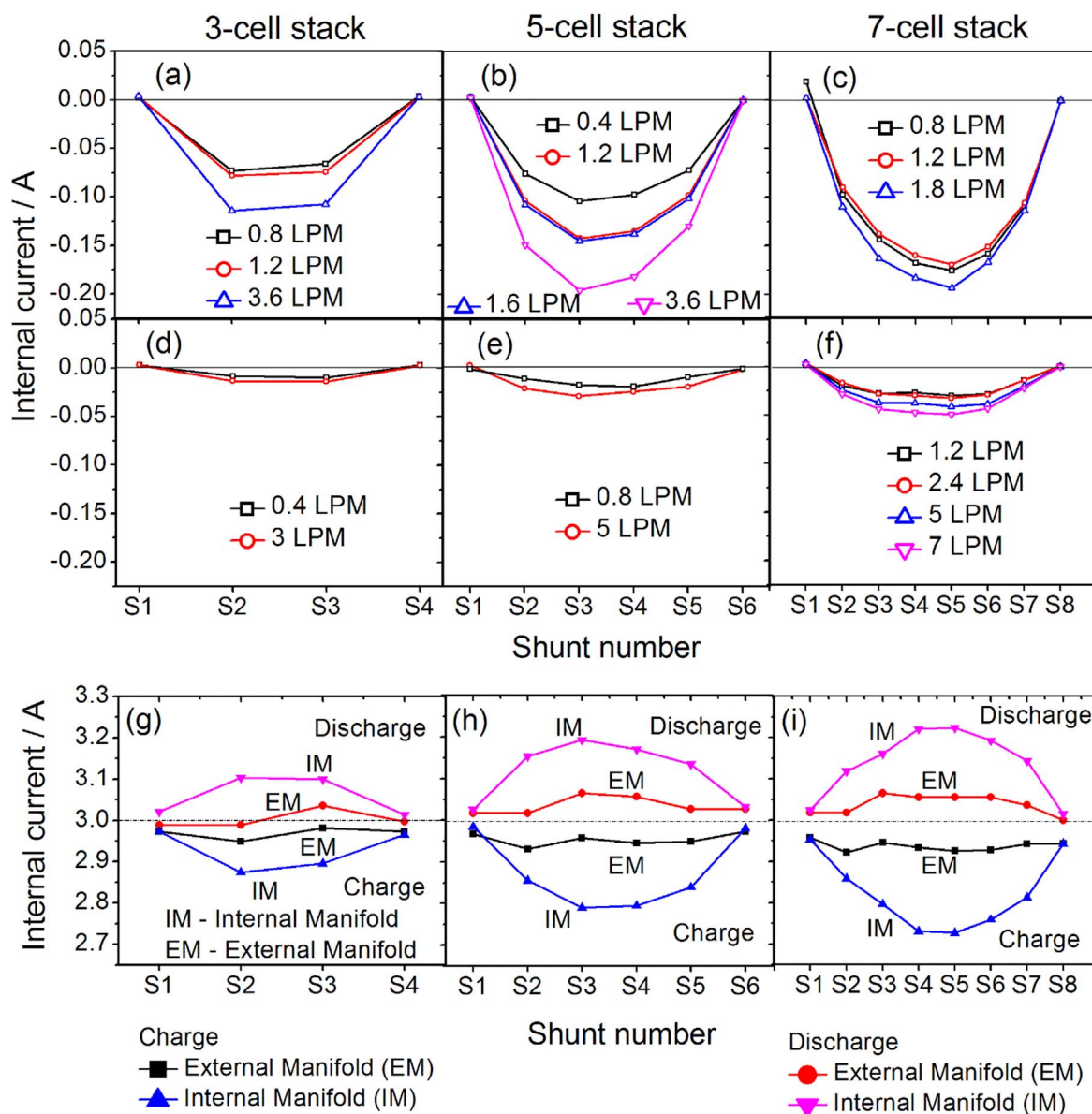

Figure 3. (a)-(f) Internal-current distribution in open-circuit condition for SLRFB with internal manifold for (a) 3-cell, (b) 5—cell and (c) 7-cell stack, and in external manifold for (d) 3-cell, (e) 5- cell and (f) 7-cell stack. (g)-(i) Comparison of internal-current distribution in 3, 5 and 7-cell stacks developed with internal and external manifold designs at 3 A charge and discharge currents with flow rate of the electrolyte being 3 lpm for 3-cell stack, 4 lpm for 5-cell stack and 1.2 lpm for 7-cell stack.

equal to—80 mA which reduces to about −15 mA at flow rate of 0.4 lpm per cell in the case of 3-cell stack with external manifold. The effect of flow rate on ionic-leakage current is also evident from the 5-cell internal manifold stack shown in Fig. 3b. In this case, the ionic-leakage current from *dc* shunt S_3 is found to be −100 mA at an overall flow rate of 0.4 lpm and increases to −200 mA at 3.6 lpm flow rate. The observation of ionic-leakage current in open circuit condition of the charged SLRFB stack mandates that the electrolyte needs to be drained out from the stack to prevent any self-discharge.

These data show that the SLRFB with external manifold performs better compared to internal manifold design. In addition to this, the internal manifold stack shows non-uniform flow of electrolyte as observed through transparent acrylic electrolyte flow frames. At times there was no flow of electrolyte through some of the cells due to airlocks in channels and the electrolyte became stagnant. Such a condition could trigger dendrites growth in the cells since dendrite formation is a diffusion-controlled process.[43] A direct impact of having shunt current in open circuit condition in the stack would cause self-discharge with middle cells being affected most.

The distribution of internal-electric current across the stack that flows from cell-to-cell as measured from *dc* shunts during charging and discharging at 3 A with internal and external manifold designs are compared in Figs. 3g–3i. Internal current distribution across the stacks at higher charge and discharge current are shown in Fig. S1 (available online at stacks.iop.org/JES/168/120552/mmedia). The electric current that flows across the *dc* shunts $S_1...S_n$ in the absence of stack is considered as background current and it is included in all the figures for the sake of comparison. According to Kirchhoff's laws of electrical circuits, the current entering a closed circuit through a junction is equal to the current leaving from the circuit through the exit junction. Hence, the current entering through the cathode of the first cell is equal to the current exit from the anode of the last cell of all the stacks while charging; during discharge the current flows in the opposite direction. It is observed that the current flow through terminal end shunts S_1 and S_n is nearly equal both during charging and discharging of the stack in the current range from 3 A to 9 A with internal and external manifold designs. At higher currents of 12 A, they are not equal indicating that a part of the ionic current could leak through the inlet/outlet of the manifold to the electrolyte-tank.

For SLRFB stacks with internal manifold design, the charging current flowing through the shunts between S_2 and S_{n-1} is lesser than the current for S_1 or S_n. Also, the discharge current flowing between S_2 and S_{n-1} shunts are higher than the currents for S_1 or S_n. This difference is due to the shunt current caused by the leakage of ionic current through the channels and manifolds. The shunt current increases as number-of-cells in the stack increases with middle cells exhibiting higher effects of the leakage current as in the case of OCP condition (see Figs. 3a–3f). In the case of stacks with external manifold, the shunt current is minimized.

From Fig. 3g, for the case of 3-cell stack with internal-manifold design, an applied charging current of 2.98 A (flowing through S_1) decreased to 2.88 A and 2.9 A across shunts S_2 and S_3, which corresponds to the bipolar connection between cell 1–2 and cell 2–3, respectively. This decrease in charge current is about 0.1 A which is 3.3% of the applied charging current respectively. As a result of this decrease in charging current, all the cells are not uniformly charged. Similarly, during discharge the applied current of 3.02 A (flowing through S_1) is found to increase to ∼3.1 A across both S_2 and S_3 indicating that 2.6% of ionic leakage current flows through the manifold triggering the middle cell to undergo discharge at higher current in relation to other two cells. However, In the case of 3-cell stack with external manifold design, the average charging current in all the cells are nearly equal and shunt current (ionic leakage current) is less than 1% in the middle cell. Similar trend is observed at higher currents for 3-cell stacks.

In case of 5-cell stack with internal manifold, the internal current distribution shows that an increase in the ionic leakage current. Figure 3h shows that the charge current of 2.98 A decreases to

2.85 A, 2.8 A, 2.8 A and 2.85 A as measured by the shunts S_2, S_3, S_4 and S_5. The decrease in charge current is about 4.3%, 6%, 6% and 4.3%. During discharge, the discharge current of 3.02 A (flowing through S_1) is found to increase by 3.15 A (4.2%), 3.2 A (5.5%), 3.17 A (4.7%) and 3.13 A (3.6%). The reduction in shunt current during discharge compared to charge is understandably due to lower voltage of stack during discharge than during charge, resulting in lower shunt current. In the case of stack with external-manifold design, there is considerable decrease in the shunt current (<1.5%).

In the case of 7-cell stack with internal manifold, Fig. 3i, the charging current of 2.95 A decreases to 2.85 A, 2.8 A, 2.7 A, 2.7 A, 2.75 A and 2.8 A as measured by the shunts S_2, S_3, S_4, S_5, S_6 and S_7, respectively. The decrease in charge current due to the ionic leakage current is 3.3%, 5%, 8.5%, 8.5%, 6.8%, and 5%. Similarly, during the discharge, the discharge current of 3.02 A (flowing through S_1) is found to increase by 3.12 A (3.3%), 3.16 A (4.6%), 3.22 A (6.6%), 3.22 A (6.6%), 3.19 A (5.6%), 3.14 A (3.97%) in the shunts S_2, S_3, S_4, S_5, S_6 and S_7, respectively. In the case of stack with external manifold, there is no such variation in charge-discharge current indicating minimum effects of ionic leakage current. Interestingly, the magnitude of shunt current at higher charge-discharge currents in the range 6 A—12 A did not increase significantly as compared to 3 A. It can be thus surmised that the stacks with internal-manifold design are affected more due to the ionic leakage-current.

Channel and manifold currents.—The sum of channel and manifold currents ($_{Ich+ma}$), as calculated from Eqs. 5 and 6 for 3,5 and 7-cell stacks of SLRFB with internal and external manifolds are shown in Figs. 4a–4i at ocp, and charge-discharge at 3 A. In the case of internal manifold design SLRFB, I_{ch+ma} of the middle cell at OCP for the 3-cell stack is about 80 mA which increases to 140 mA for 5-cell stack and 170 mA for 7-cell stack. I_{ch+ma} currents are found to be 90 mA, 95 mA and 245 mA, respectively, for the 3, 5 and 7-cell stacks during charging at 3 A. During discharge, I_{ch+ma} is observed to be 95 mA, 100 mA and 150 mA, respectively. The effect of shunt current is more evident from 7-cell stack. The magnitude of the channel and manifold current is higher at charging than at discharging. In the case of external manifold design SLRFB, the total I_{ch+ma} is found to be relatively invariant at OCP and is much lower than that for the internal manifold design stack. In the case of 5 and 7-cell stack during discharge the I_{ch+ma} is found to be about 50 mA.

The ionic leakage current through each cell as obtained from Eqs. 7 and 8 for 3,5 and 7-cell SLRFB stacks with internal and external manifold designs at OCP, and during charging and discharging at 3 A are shown in Figs. 5a–5i. The ionic leakage current or shunt current in the case of external manifold SLRFB is reduced as compared to the internal manifold designs; it is close to zero for the middle cell in all SLRFB stacks. Also, the ionic leakage current from side cells is found to increase with increase in the size of stack with external manifold design.

Current—potential performance of the membrane-less SLRFB stacks.—The stacks of 3-cell, 5-cell and 7-cell with internal and external manifold designs are first activated by few cycles of charge at constant current density of 24 mA cm^{-2} for 1 h and discharge to 0.8 V per cell. Subsequently, the stacks are charged at 24 mA cm^{-2} for 1 h, and then their current—potential performance behavior is recorded by galvanostatic polarization method (Fig. 6). The 3-cell (Fig. 6a) and 5-cell (Fig. 6b) stacks of SLRFB with internal manifold design show a maximum power density of 33 mW cm^{-2} and 37.5 mW cm^{-2}, respectively. In the case of 7-cell stack, it is decreased to about 15 mW cm^{-2} (Fig. 6c). Interestingly, the maximum power density in the case of external manifold design is found to be nearly equal to 50 mW cm^{-2} indicating that the stack with external manifold design has no significant loss in performance due to ionic leakage-current.

Galvanostatic charge-discharge studies.—The IR-corrected galvanostatic charge-discharge cycles for the 3,5 and 7-cell SLRFB
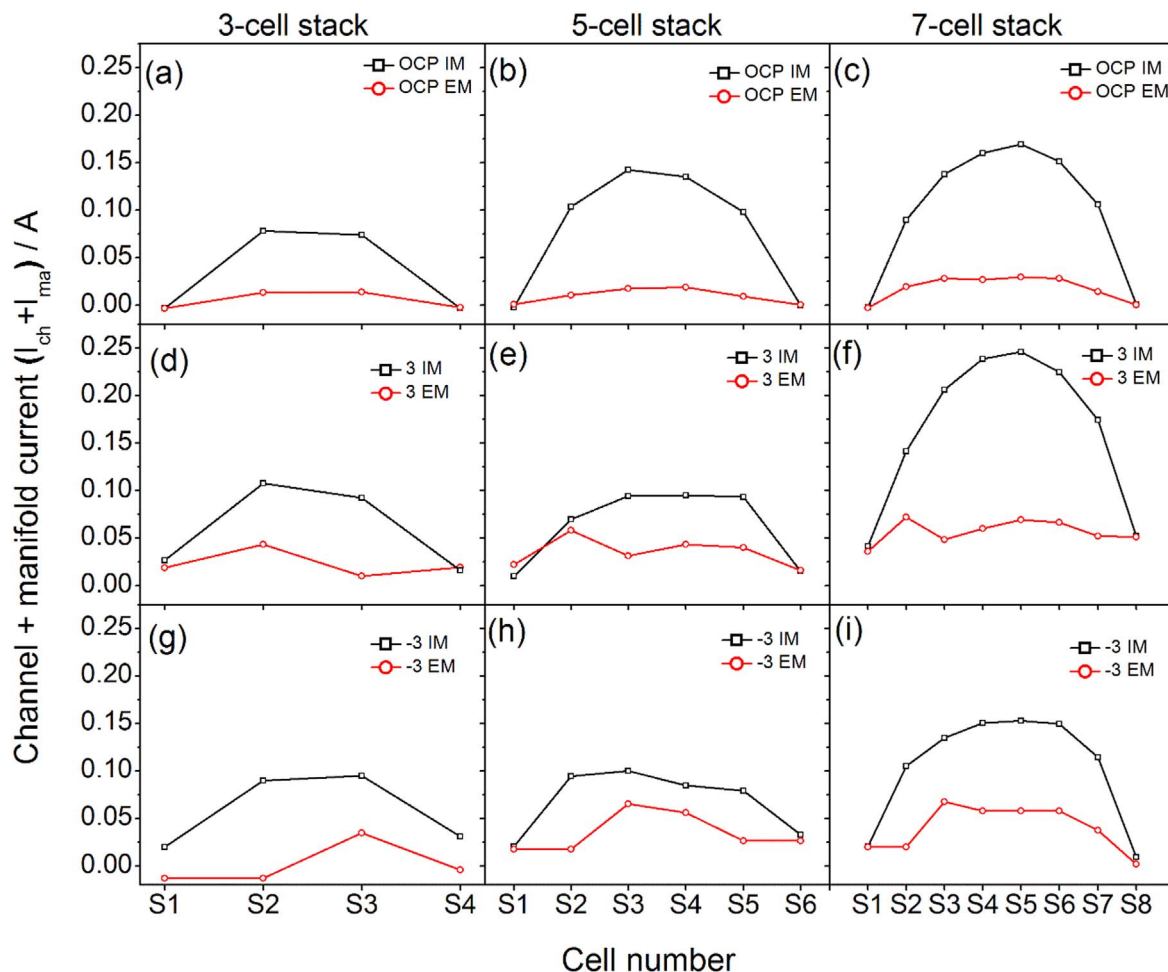
Figure 4. The channel and manifold current in 3, 5, and 7-cells stacks of SLRFB with internal and external manifolds. Figs.(a)–(c) in open circuit, Figs. (d)–(f) show while charging at 3 A and Figs. (g)–(i) during discharge at 3 A for stacks of SLRFB with internal and external manifolds with flow rate of the electrolyte being 3 lpm for 3-cell stack, 4 lpm for 5-cell stack and 1.2 lpm for 7-cell stack.

stacks with internal and external manifold designs are shown in Fig. S2. In the case of stacks with internal manifold design, 3-cell and 5-cell stacks could be cycled for 30 min charge durations whereas the 7-cell stack is able to be cycled for 15 min durations only. At longer charge durations, like 1 h, the stacks are found to fail during cycling due to the accumulation of active materials at first and last cells of the stack and some sludge is found to be floating in the electrolyte. Figure S2a show the charge-discharge curves for 3-cell stack when charged for 30 min at 24 mA cm^{-2} current density and discharged to 1.5 V. Figure 7a shows individual cell discharge performance data for 3—cell stack. The individual cell discharge data indicate that the middle cell, (cell 2), suffers deeper discharge as compared to cell 1 and cell 3. This indicates that middle cell undergoes concentration polarization towards the end of discharge indicating the presence of less active material caused by the ionic leakage current. Figure S2b shows the charge-discharge performance behavior for the 5-cell stack when charged for 30 min at 24 mA cm^{-2} along with the individual cell performance. The stack is discharged to cut-off voltage of 4 V. The individual cell discharge data for the 5-cell stack are shown in Fig. 7b. It is observed that the middle cell undergoes deeper discharge.

The charge-discharge data for 7-cell stack are shown in Fig. S2c along with individual cell charge-discharge data. The stack was charged for 15 min duration and discharged to cut-off voltage of 5.6 V. The 7-cell stack with internal manifold design was able to be charged only 15 min durations and exhibits low cycle-life. At higher charge durations, the middle cell fails quickly due shunt current. The individual cell discharge data for the 7—cell stack is shown in

Fig. 7c. Individual cell discharge data show that the middle cells polarize more and undergo deep discharge compared to end cells due to higher ionic leakage current in the former. Figures S2d-S2e shows the charge-discharge performance data for 3, 5 and 7-cell stacks with external manifold design. All the three stacks are charged for 1 h at 24 mA cm^{-2} and discharged to 2.4 V, 4.0 V and 5.6 V, respectively. Interestingly, the discharge data for the individual cells presented in Figs. 7d–7e for 3,5,7-cell stacks with external manifold show nearly uniform performance, indicating uniform state of charge due to lower shunt current effect across the cells of the stack.

Performance characteristics of an 8-cell membrane-less SLRFB stack of 12 V/250 Wh.—The 8-cell membrane-less SLRFB stack developed with external manifold design is first activated by charge-discharge cycles at 24 mA cm^{-2} current density for 1 h duration with 7.2 V cutoff voltage. After about 40 charge-discharge cycles of activation, the battery is tested for its cyclability, current—potential characteristic and long duration charge-discharge schedules. The open-circuit voltage of the battery in charged state is about 13.5 V and is about 13.0 V in discharged state. The current—potential performance data for the 8-cell stack for different charge durations of 30 min. 1 h, 1.5 h and 2 h at 24 mA cm^{-2} current density are shown in Fig. 8a. The maximum power that can be drawn from the battery increases with the increasing charge durations. The input capacity of the battery when charged for 30 min is 6 Ah and is 24 Ah for 2 h charge duration. The maximum power is about 175 W when charged for 30 min and is 233 W when charged for 2 h. The battery is subjected to charge-discharge cycles at 24 mA cm^{-2}
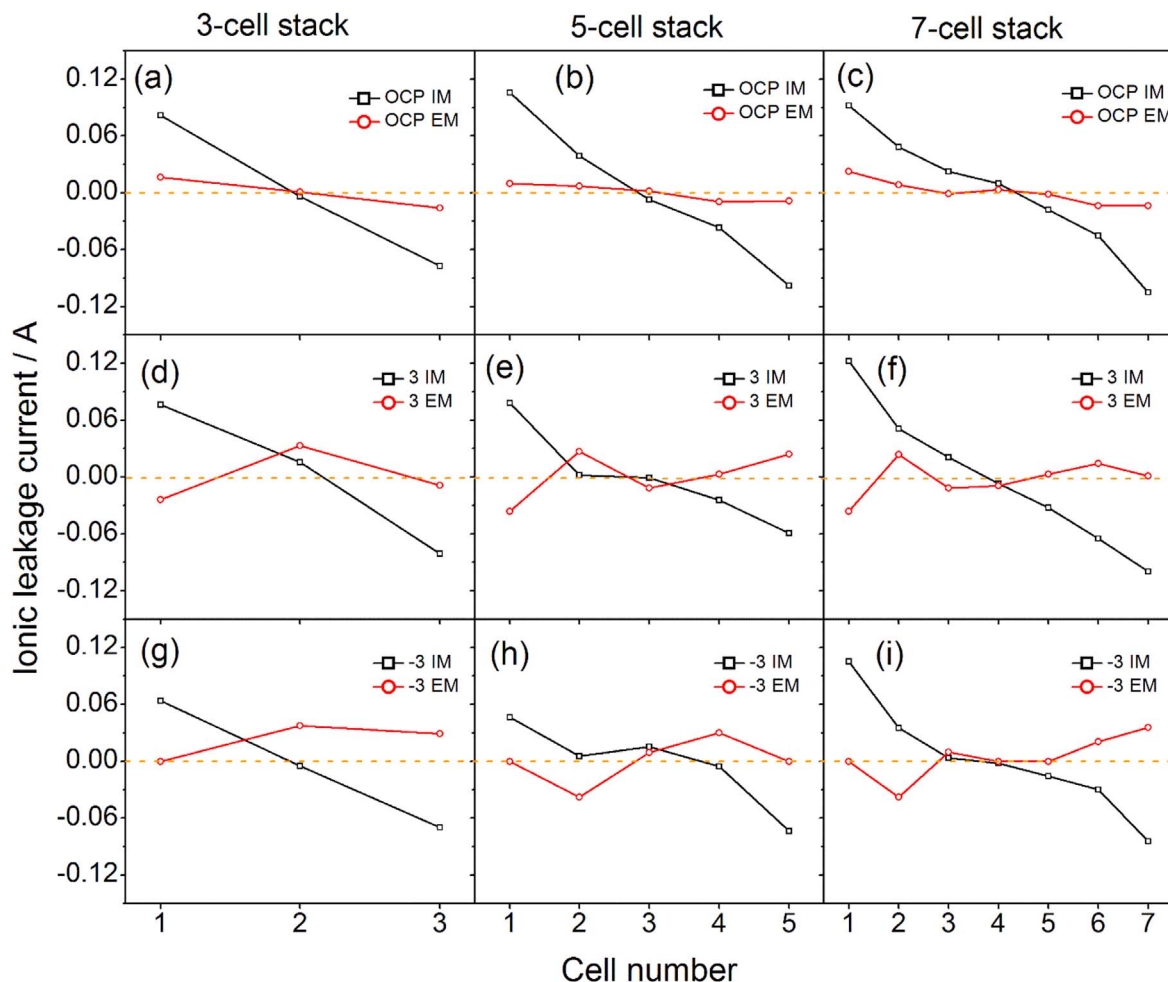
Figure 5. The ionic leakage current in 3, 5, and 7-cells stacks of SLRFB with internal and external manifolds. Figs.(a)–(c) in open circuit, Figs. (d)–(f) show while charging and Figs. (g)–(i) during discharge stacks of SLRFB with internal and external manifolds with flow rate of the electrolyte being 3 lpm, 4 lpm and 1.2 lpm for 3,5 and 7-cell stacks respectively.
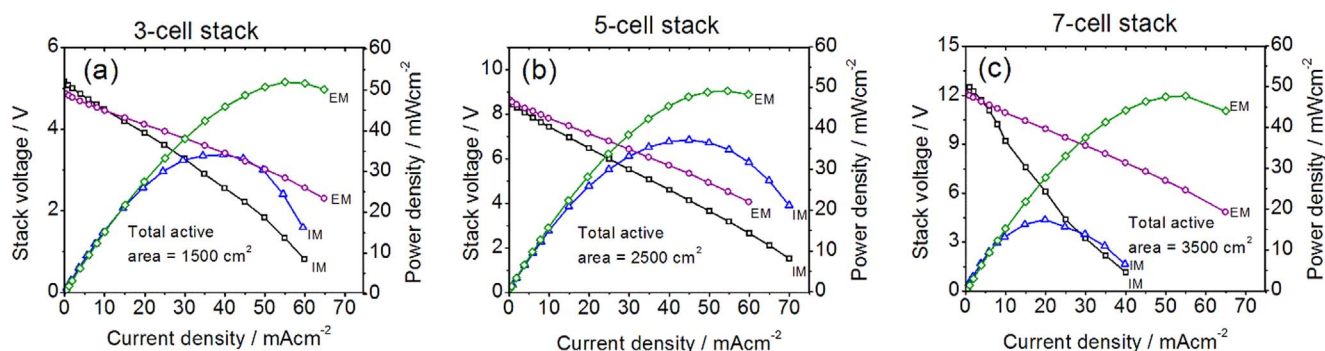

Figure 6. Steady state current—potential data obtained by constant-current method after charging for 1 h at 24 mA cm^{-2} current density for 3,5 and 7-cell stacks with internal manifold at flow rates of 0.4 lpm, 0.6 lpm and 1.2 lpm, respectively and for stacks with external manifold design at flow rates of 3 lpm, 5 lpm and 7 lpm, for 3,5 and 7-cell stacks respectively.

current density for 1 h duration to test its cyclability. The charge-discharge data for all 100 cycles is shown in Fig. 8b and for 100th cycle along with its individual cell performance are shown in Fig. 8c. The OCV of the battery at the end of 99th cycle is 13.0 V and, on charge, initially increases to about 18 V and subsequently decreases to 17 V. It is also observed that the individual cells exhibit almost uniform behavior during charge-discharge of the battery and there is no significant effect of shunt current under the present design and on working of the battery. The coulombic efficiency, voltaic

efficiency, and energy efficiency for these 100 cycles are presented in Fig. 8d. The battery voltage in its first cycle of charge is close to 20 V and the spike in initial charging voltage decreases gradually with increasing number of cycles. However, the initial spike in charge voltage appears again after 25 cycles but the battery voltage rises only to about 18 V. The battery clearly shows a good cyclability for 100 charge-discharge cycles. The coulombic efficiency in the first cycle is close to 60% which increases to about 95% over 25 cycles. Since the initial spike in the charge curve starts
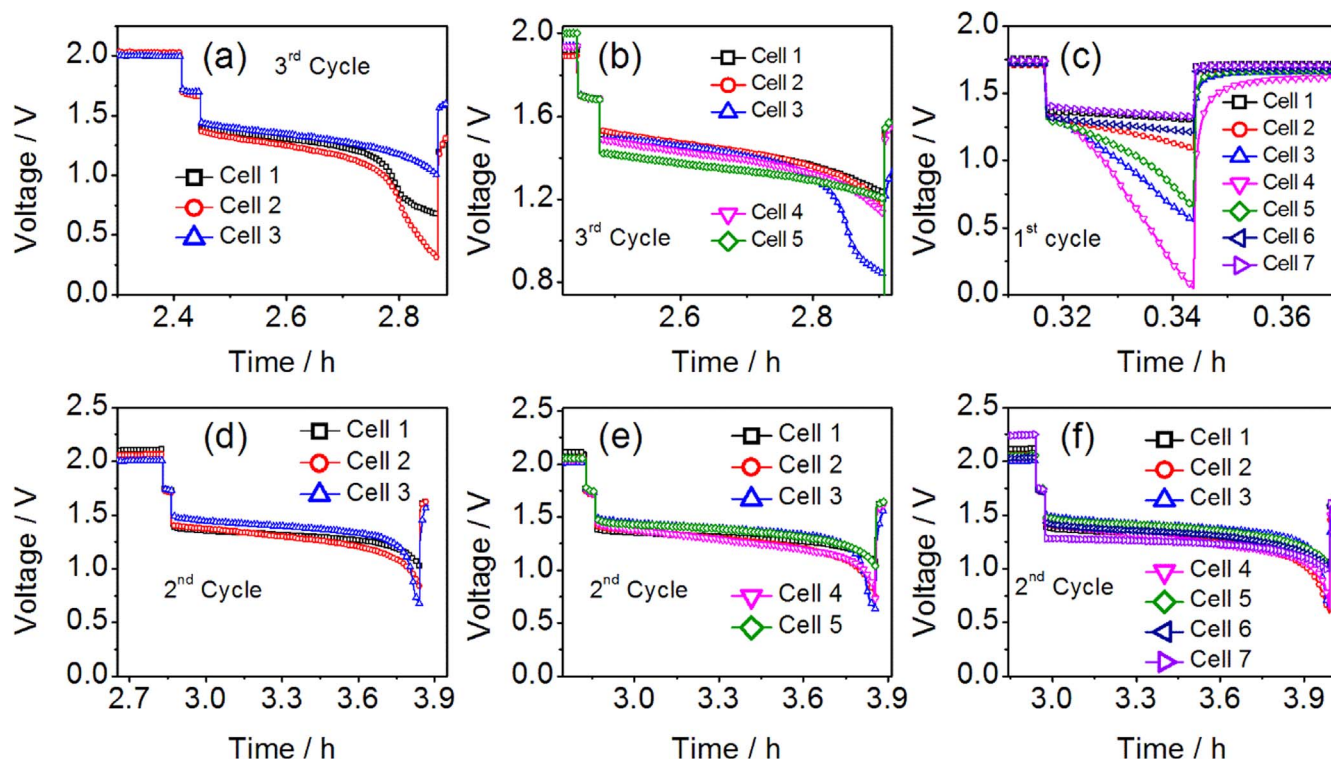
Figure 7. Typical discharge curves at 24 mA cm^{-2} current density for 3, 5, and 7-cell stacks with internal manifold (a)–(c) and external manifold (d)–(f) designs.

appearing after the coulombic efficiency reaches >95%, this initial rise is again due to the nucleation overpotential associated with the deposition of active materials.

The voltaic efficiency of the battery in its first cycle is found to be about 45% and increases to 55% over 25 cycles. The low voltaic efficiency is attributed to the internal resistance of stack caused due to the use of untreated graphite felt, impervious graphite plates and activation overpotential associated with cathode reaction. The energy efficiency is calculated to be 28% in the first cycle which increases to 50% in 25 cycle due to the increase in coulombic and voltaic efficiencies. The input capacity of the battery is further increased to 27 Ah by charging it at 18 mA cm^{-2} for 3 h and discharging at constant power of 50 W up to 6.4 V cutoff.

Figure 8e illustrates the charge-discharge voltage profiles of the battery when charged at 18 mA cm^{-2} for 3 h and discharged at constant power of 50 W. Long period charge-discharge cycles of stack is continued till 20 cycles. The average discharge capacity observed is 25 Ah with average faradaic efficiency of about 94%. Typically, for 5th cycle, the input energy is 426 Wh while output energy is 273 Wh which shows the energy efficiency to be about 64%. The charge, voltage and energy efficiency data are presented in Fig. 8f. When the battery is charged with 20 mA cm^{-2} for 3 h, the charge data show a rise in voltage towards the end-of-charge indicating oxygen evolution. These data suggest that increasing the capacity of battery for more than 25 Ah results in some loss of charge efficiency due to oxygen evolution reaction. Since the mechanism of the electrode reactions involves precipitation—dissolution of active materials, its specific capacity depends on the quantity of active material deposited per unit area which is defined in the units of mAh cm^{-2}. It is surmised that the maximum capacity of the battery is 25 Ah and the corresponding specific capacity is 50 mAh cm^{-2}.

Conclusions

The ramifications of shunt current in membrane-less SLRFB with internal and external manifold designs are studied by developing befittingly designed 3, 5 and 7-cell stacks with provision to measure

the internal current distribution using high-precision *dc* shunts. Shunt current is observed in open-circuit condition of the SLRFB in charged state when electrolyte is circulated. Hence, it is mandatory to drain out the electrolyte to prevent any loss in capacity after charging the battery. It is observed that the shunt current increases with stack size and in the case of stacks with internal manifold design during charging at 3 A, the charge current in the middle cell decreases to 3.3%, 6% and 8.5% for 3, 5 and 7-cell stacks, respectively, as compared to other cells. Furthermore, during discharging at 3 A, the discharge current of the middle cell increases by 2.6%, 5.5%, and 6.6% for 3, 5 and 7-cell stacks, respectively. This creates imbalance in the state of charge of cells within the stack. There is no such adverse effect observed with stacks of external manifold design. The shunt current increases with increase in electrolyte flow rate for the case of internal manifold but in the case of external manifold, it remains almost invariant. The current—potential polarization studies show that while the single cell, 3-cell and 5-cell stacks delivered a maximum power density of 35 mW cm^{-2}, it is declined to 15 mW cm^{-2} for the 7-cell stack with internal manifold design; the power density remains almost invariant at 50 mW cm^{-2} for the stacks with external manifold design.

To account for the beneficial role of external manifold design for the SLRFB stack, a novel serially connected 8—cell membrane-less SLRFB stack is designed, developed and demonstrated with its performance characteristics. The battery is developed with external manifold design to overcome adverse effects of shunt current. The OCV of the battery is 13.5 V and it can store about 250 Wh of energy. The battery is tested at varying charge-discharge load current-densities between 6 mA cm^{-2} and 24 mA cm^{-2} for varying charge durations of 30 min, to 3 h. The battery is found to be capable of storing a maximum of 50 mAh cm^{-2} specific capacity when charged at 18 mA cm^{-2} for a duration of 3 h and discharged galvanostatically at 10 mAcm^2. The battery delivers a maximum power of ~230 W when charged for 2 h at 24 mA cm^{-2} current density and can store about 250 Wh energy when charged for 3 h at 18 mA cm^{-2}. The battery shows excellent cyclability over 100
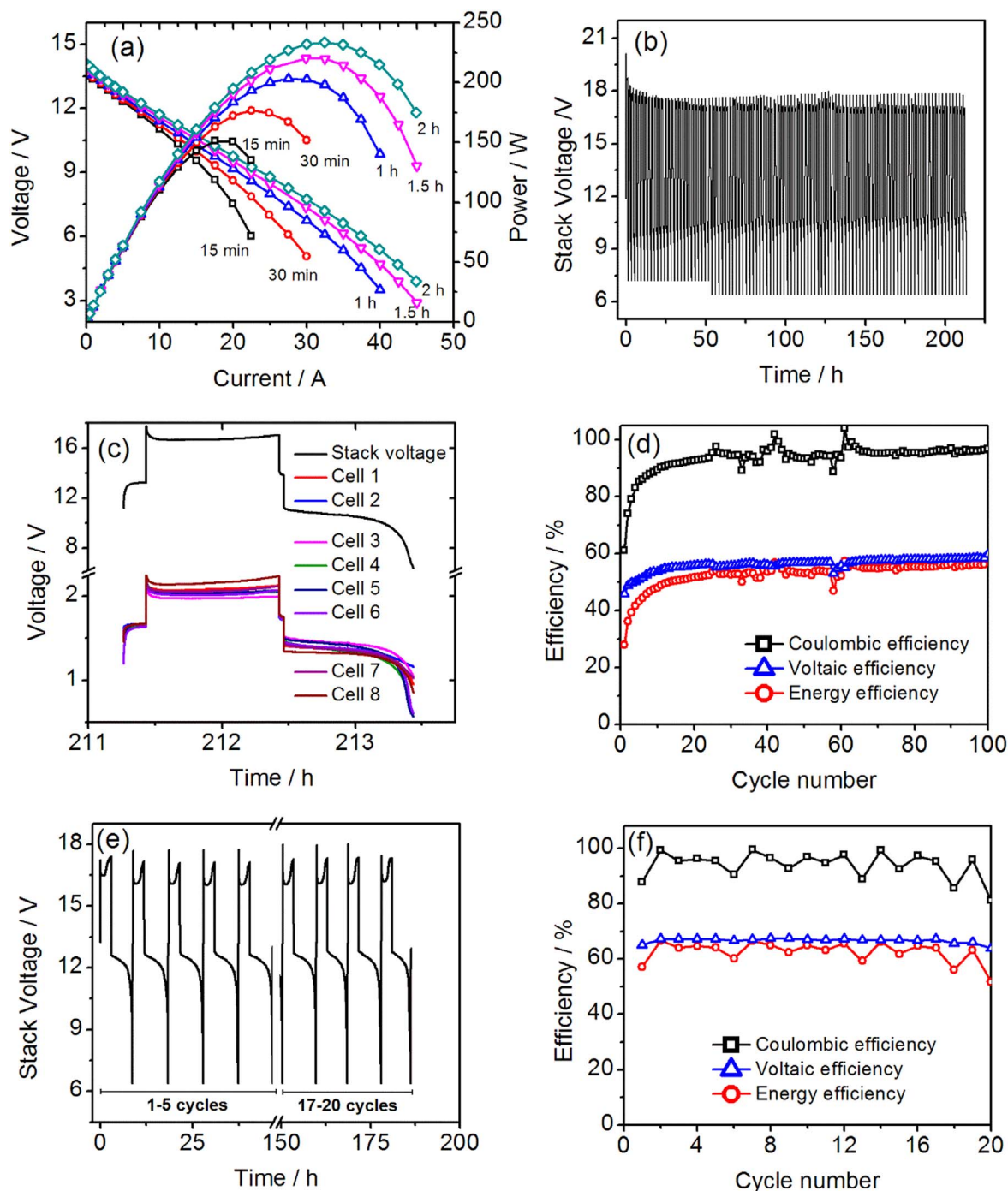
Figure 8. (a) Current-potential data for the 8-cell stack of SLRFB after charging for varying durations. (b) Constant current (24 mA cm^{-2} current density), 1 h charge-discharge performance of the 8-cell stack for 100 cycles. (c) Charge-discharge profile of stack and individual cells for 100th cycle. (d) The charge, voltaic and energy efficiencies for 100 charge-discharge cycles. (e) The charge-discharge voltage profile of the battery when charged at 9 A (18 mA cm^{-2} current density) for 3 h and discharged at constant power of 50 W. The corresponding charge, voltaic and energy efficiencies during long period charge-discharge schedules are shown in (f).

cycles with a coulombic efficiency of 95%, voltaic efficiency of 55% and energy efficiency of 52%.

Since the faradaic efficiency of the SLRFB is always less than 100% due the inherent nature of the oxygen evolution reaction at cathode, its periodic maintenance is necessary. Since different cells exhibit different faradaic efficiencies over repeated charge—discharge schedules, the state-of-charge on individual electrodes is different as it is difficult to do the maintenance independently on each cell. The present SLRFB stack overcomes this problem with its novel design of individual electrode tags out of the stack for

connections. This helps to change the series connected cells into parallel which reduces the multiple cell stack into a single cell and one can discharge the entire stack with single step deep discharge to bring back the stack near initial condition. Subsequently, the stack can be connected back in series. Such a novelty is not reported in any other redox-flow -battery systems, particularly in SLRFB, to the best of our knowledge. It is notable that the materials and engineering factors are not fully optimized, and hence further improvements are highly likely.

ORCID

M. K. Ravikumar https://orcid.org/0000-0002-3773-3895
A. K. Shukla https://orcid.org/0000-0001-6091-2237

References

1. T. M. Gür, *Energy Environ. Sci.*, **11**, 2696 (2018).
2. The Paris agreement. United Nations Climate Change, (https://unfccc.int/process-and-meetings/the-paris-agreement/the-paris-agreement) (2015).
3. Research and Markets. Grid-Scale Battery Storage Technologies Market by Battery, by Application - Global Opportunity Analysis and Industry Forecast, 2020—2030, 5215123 (https://researchandmarkets.com/reports/5215123/ grid-scale-battery-storage-technologies-market-by), 2020.
4. B. Dunn, H. Kamath, and J. M. Tarascon, *Science*, **334**, 928 (2011).
5. E. Sánchez-Díez, E. Ventosa, M. Guarnieri, A. Trovò, C. Flox, R. Marcilla, F. Soavi, P. Mazur, E. Aranzabe, and R. Ferret, *J. Power Sources*, **481**, 228804 (2021).
6. M. L. Perry and A. Z. Weber, *J. Electrochem. Soc.*, **163**, A5064 (2015).
7. Energy Storage Grand Challenge, *Energy Storage Market Report* (U.S. Department of Energy) (2020), NREL/TP-5400-78461 (https://energy.gov/energy-storage-grand-challenge/downloads/energy-storage-market-report-2020).
8. M. Skyllas-Kazacos, M. H. Chakrabarti, S. A. Hajimolana, F. S. Mjalli, and M. Saleem, *J. Electrochem. Soc.*, **158**, R55 (2011).
9. A. Z. Weber, M. M. Mench, J. P. Meyers, P. N. Ross, J. T. Gostick, and Q. Liu, *J. Appl. Electrochem.*, **41**, 1137 (2011).
10. A. Hazza, D. Pletcher, and R. Wills, *Phys. Chem. Chem. Phys.*, **6**, 1773 (2004).
11. D. Pletcher and R. Wills, *Phys. Chem. Chem. Phys.*, **6**, 1779 (2004).
12. D. Pletcher and R. Wills, *J. Power Sources*, **149**, 96 (2005).
13. A. Hazza, D. Pletcher, and R. Wills, *J. Power Sources*, **149**, 103 (2005).
14. D. Pletcher, H. Zhou, G. Kear, C. T. J. Low, F. C. Walsh, and R. G. A. Wills, *J. Power Sources*, **180**, 621 (2008).
15. D. Pletcher, H. Zhou, G. Kear, C. T. J. Low, F. C. Walsh, and R. G. A. Wills, *J. Power Sources*, **180**, 630 (2008).
16. X. Li, D. Pletcher, and F. C. Walsh, *Electrochim. Acta*, **54**, 4688 (2009).
17. J. Collins, G. Kear, X. Li, C. T. J. Low, D. Pletcher, R. Tangirala, D. Stratton-Campbell, F. C. Walsh, and C. Zhang, *J. Power Sources*, **195**, 1731 (2010).
18. J. Collins, X. Li, D. Pletcher, R. Tangirala, D. Stratton-Campbell, F. C. Walsh, and C. Zhang, *J. Power Sources*, **195**, 2975 (2010).
19. A. Oury, A. Kirchev, and Y. Bultel, *J. Power Sources*, **264**, 22 (2014).
20. P. Leung, X. Li, C. P. de León, L. Berlouis, C. T. J. Low, and F. C. Walsh, *RSC Adv.*, **2**, 10125 (2012).
21. M. K. Ravikumar, S. Rathod, N. Jaiswal, S. Patil, and A. Shukla, *J. Solid State Electrochem.*, **21**, 2467 (2017).
22. F. Beck, *US Patent*, No. 4001037 (1977).
23. J. Cheng, C. Gao, Y. H. Wen, J. Q. Pan, Y. Xu, and G. P. Cao, *International Journal Energy Science (IJES).*, **3**, 165 (2013).
24. D. Pletcher, *ECS Trans.*, **28**, 1 (2010).
25. R. G. A. Wills, J. Collins, D. Stratton-Campbell, C. T. J. Low, D. Pletcher, and F. C. Walsh, *J. Appl. Electrochem.*, **40**, 955 (2010).
26. M. Krishna, E. J. Fraser, R. G. A. Wills, and F. C. Walsh, *J. Energy Storage.*, **15**, 69 (2018).
27. Y. T. Lin, H. L. Tan, C. Y. Lee, and H. Y. Chen, *Electrochim. Acta*, **263**, 60 (2018).
28. A. Oury, A. Kirchev, Y. Bultel, and E. Chainet, *Electrochim. Acta*, **71**, 140 (2012).
29. M. Lanfranconi and H. J. Lilienthal, *J. Sustain. Dev. Energy Water Environ. Syst.,*, **7**, 343 (2019).
30. J. Guk, M. Hyeong-seop, O. Young-je, and L. Jae-gap, *Patent No.*, KR101009440B1 (2010).
31. L. F. Arenas, C. Ponce de León, and F. C. Walsh, *J. Energy Storage.*, **11**, 119 (2017).
32. P. R. Prokopius, *NASA Technical Memorandum*, NASA TM X-3359 (1976).
33. M. Skyllas-Kazacos, J. McCann, Y. Li, J. Bao, and A. Tang, *Chemistry Select.*, **1**, 2249 (2016).
34. R. E. White, C. W. Walton, H. S. Burney, and R. N. Beaver, *J. Electrochem. Soc.*, **133**, 485 (1986).
35. E. A. Kaminski and R. F. Savinell, *J. Electrochem. Soc.*, **130**, 1103 (1983).
36. H. S. Burney and R. E. White, *J. Electrochem. Soc.*, **135**, 1609 (1988).
37. H. N. Seiger, *J. Electrochem. Soc.*, **133**, 2002 (1986).
38. D. Pletcher and F. C. Walsh, *Industrial Electrochemistry* (Chapman and Hall, London) 2nd ed.138 (1990).
39. T. F. O'Brien, T. V. Bommaraju, and F. Hine, *Handbook of Chlor-Alkali Technology* (Springer, New York, NY) 1, 391 (2005).
40. A. K. Shukla, S. Patil, M. K. Ravikumar, and S. Rathod, *Indian Patent application number.*, 202141001976 (2021).
41. R. Suman, *Studies on Soluble Lead Redox Flow Battery, PhD Thesis*, Indian Institute of Science, Bangalore (2021), https://etd.iisc.ac.in/handle/2005/5139.
42. A. B. Velichenko and D. Devilliers, *J. Fluor. Chem.*, **128**, 269 (2007).
43. N. D. Nikolić, K. I. Popov, P. M. Živković, and G. Branković, *J. Electroanal. Chem.*, **691**, 66 (2013).
44. A. S. Aricò, V. Antonucci, N. Giordano, A. K. Shukla, M. K. Ravikumar, A. Roy, S. R. Barman, and D. D. Sarma, *J. Power Sources*, **50**, 295 (1994).